

Phonon effects on x-ray absorption and nuclear magnetic resonance spectroscopies

Ruidy Nemausat,^{1,2,*} Delphine Cabaret,¹ Christel Gervais,² Christian Brouder,¹

Nicolas Trcera,³ Amélie Bordage,⁴ Ion Errea,^{5,6} and Francesco Mauri¹

¹*Sorbonne Universités, UPMC Univ Paris 06, Institut de Minéralogie,
de Physique des Matériaux et de Cosmochimie (IMPMC),
UMR CNRS 7590, 4 place Jussieu, F-75005, Paris, France*

²*Sorbonne Universités, UPMC Univ Paris 06, Laboratoire de Chimie de la Matière Condensée de Paris (LCMCP),
UMR CNRS 7574, Collège de France, 11 place Marcelin Berthelot, F-75005 Paris, France*

³*Synchrotron SOLEIL, L'Orme des Merisiers, St Aubin, BP 48, F-91192 Gif sur Yvette, France*

⁴*Université Paris-Sud, Institut de Chimie Moléculaire et des Matériaux d'Orsay (ICMMO),
UMR CNRS 8182, 15 rue du doyen Georges Poitou, F-91400, Orsay, France.*

⁵*Fisika Aplikatua 1 Saila, EUITI, University of the Basque Country (UPV/EHU),
Rafael Moreno "Pitxitri" Pasealekua 3, 48013 Bilbao, Basque Country, Spain*

⁶*Donostia International Physics Center (DIPC), Manuel Lardizabal Pasealekua 4,
20018 Donostia-San Sebastián, Basque Country, Spain*

(Dated: September 18, 2015)

In material sciences, spectroscopic approaches combining *ab initio* calculations with experiments are commonly used to accurately analyze the experimental spectral data. Most state-of-the-art first-principle calculations are usually performed assuming an equilibrium static lattice. Yet, nuclear motion affects spectra even when reduced to the zero-point motion at 0 K. We propose a framework based on Density-Functional Theory that includes quantum thermal fluctuations in theoretical X-ray Absorption Near-Edge Structure (XANES) and solid-state Nuclear Magnetic Resonance (NMR) spectroscopies and allows to well describe temperature effects observed experimentally. Within the Born-Oppenheimer and quasi-harmonic approximations, we incorporate the nuclear motion by generating several non-equilibrium configurations from the dynamical matrix. The averaged calculated XANES and NMR spectral data have been compared to experiments in MgO, proof-of-principle compound. The good agreement obtained between experiments and calculations validates the developed approach, which suggests that calculating the XANES spectra at finite temperature by averaging individual non-equilibrium configurations is a suitable approximation. This study highlights the relevance of phonon renormalization and the relative contributions of thermal expansion and nuclear dynamics on NMR and XANES spectra on a wide range of temperatures.

I. INTRODUCTION

X-ray Absorption Near-Edge Structure (XANES)¹ and solid-state Nuclear Magnetic Resonance (NMR)² spectroscopies are powerful probes of the electronic and local structure of inorganic materials. The combination of these two techniques provides a deep understanding of the electronic and structural properties of materials. For instance, a recent study coupling X-ray absorption spectroscopy and NMR successfully resolved the local structure of Al sites in zeolites.³ The noticeable improvements in methodology and instrumentation resulted in a spectacular enhancement of the quality and resolution of spectra for both techniques.⁴⁻⁷ Nonetheless, the huge amount of information contained in experimental spectra makes their accurate assignment difficult. To address this difficulty theoretical tools are used beforehand or in conjunction with experimental data.⁸⁻¹⁰

Most first-principle calculations in the solid-state consider the nuclei fixed at their equilibrium positions, as obtained by X-ray or neutron diffraction. However, atoms are subjected to quantum thermal fluctuations, which reduce to the zero-point motion at the absolute zero (0 K). Temperature-dependent experiments exhibit significant variations of spectroscopic properties, such as chemical shifts,^{11,12} relaxation times,¹³ and Electric Field

Gradient values¹⁴⁻¹⁷ (EFG) measured by NMR or the pre-edge structures observed in XANES spectra of oxide materials.¹⁸⁻²⁰ In the case of NMR, it has been observed that the chemical shifts vary of several ppm when temperature increases over thousands of degrees.^{11,12} The EFG tensor is also very sensitive to temperature and nuclear quadrupole resonance experiments have shown a variation of the resonances frequencies $\nu_{\pm,0}$ up to -0.2 kHz.K^{-1} .^{14,15} In the case of XANES spectroscopy, it has been recently shown that the intensity and position of the pre-edge peak highly depend on temperature.¹⁸⁻²⁰ It has been demonstrated that the pre-edge structure is due to a violation of symmetry induced by the quantum thermal fluctuations. For instance, at the Al *K*-edge of various oxides, the nuclear motion is responsible for the appearance of a pre-edge peak corresponding to the $1s \rightarrow 3s$ forbidden electronic transitions.²⁰⁻²²

Multiple attempts to theoretically reproduce the lattice dynamical effects in solid-state spectroscopies have emerged in the literature. Pioneering approaches based on averaging the chemical shielding tensors over different orientations of mobile species were proposed to include nuclear motion in NMR calculations.^{23,24} In parallel, it was shown that small displacements of either the absorbing atom^{20,21,25} or the $1s$ initial wave function in the crude Born-Oppenheimer approximation²²

could reveal forbidden transitions in K -edge XANES spectra. Although quite promising, these methods do not account for the collective lattice dynamics. A substantial theoretical work proved that vibrations could be represented as the convolution of the x-ray absorption cross section, calculated for the equilibrium configuration, with the phonon spectral function.^{26,27} This theory has been applied to reproduce room-temperature experimental XANES spectra in Ref. 20. In the case of non-quantum nuclear motion, the method of choice would be Molecular Dynamics (MD) at finite temperature, either classical or *ab initio*. In NMR, *ab initio* MD was used to study the dependence on temperature of the chemical shift^{12,28–31} and quadrupolar relaxation rates^{13,32} but mostly in organic compounds. MD calculations were also used in XANES to calculate Li and S K -edges XANES spectra of Li-ion batteries at room temperature^{33,34} or the Al and Fe K -edges in warm dense plasmas.^{35–37} However, MD consider the vibrations as a classical phenomenon and is therefore appropriate only if $k_B T > \hbar \varpi_{vib}$, with ϖ_{vib} the vibration frequency.³⁸ To account for the quantum behavior of vibrations, Path Integral Molecular Dynamics (PIMD) was used to simulate NMR³⁹ and C K -edge NEXAFS⁴⁰ spectra in organic compounds. In both spectroscopies, the results were improved using PIMD, but at the cost of a larger statistical error. Seeking for computationally less expensive methods, Monte Carlo sampling has been used to account for the vibrational effects on the chemical shifts in MgO⁴¹ and recently a more computationally efficient method arose by assuming a quadratic coupling between vibrations and the shielding tensor.⁴² The Monte Carlo sampling method was also used to simulate XANES spectra of molecules in solutions,⁴³ but, to our knowledge, it has not been applied to inorganic solids yet.

The purpose of this work is to describe quantum thermal fluctuations, using methods based on Density-Functional Theory (DFT).⁴⁴ In the Born-Oppenheimer (BO)⁴⁵ and Quasi-Harmonic Approximation (QHA),^{46,47} the thermal effects are modeled by generating atomic position configurations obeying quantum statistics at finite temperatures. The theoretical work is confronted to NMR and recently acquired XANES temperature-dependent experiments for our proof-of-principle compound MgO. This ionic oxide has been chosen for three main reasons: (i) its rock salt structure is ideal to observe thermal effects as its lattice constant is the only free parameter, (ii) it shows no phase transition up to its melting point around 3250 K,⁴⁸ allowing a wide temperature range for experimental measurements, (iii) multiple theoretical studies demonstrated that the harmonic behavior of MgO remains at temperature as high as 1500 K and its Debye temperature has been found, theoretically, to be about 941 K.^{49–51}

The paper is structured as follows. In Sec. II, the formalism upon which our theoretical model is based is detailed. In Sec. III, experimental and computational details are given. In Sec. IV, experimental and theoretical

results obtained on MgO are presented and discussed. Finally, the conclusions of this work are drawn in Sec. V.

II. FORMALISM

A. Quasi-harmonic vibrations

A crystal can be seen as a system of N nuclei and N_e electrons with respective position vectors $(\mathbf{R}_1, \dots, \mathbf{R}_N)$ and $(\mathbf{r}_1, \dots, \mathbf{r}_{N_e})$. The collective coordinates $\bar{\mathbf{R}} = (\mathbf{R}_1, \dots, \mathbf{R}_N)$ and $\bar{\mathbf{r}} = (\mathbf{r}_1, \dots, \mathbf{r}_{N_e})$ are used thereafter. The stationary states of the system are described by the wave function $\Psi(\bar{\mathbf{r}}, \bar{\mathbf{R}})$ solution of the following general Schrödinger equation,

$$(T_N + T_e + V_e + V_{e-N} + V_N) \Psi(\bar{\mathbf{r}}, \bar{\mathbf{R}}) = E \Psi(\bar{\mathbf{r}}, \bar{\mathbf{R}}), \quad (1)$$

with T_N the kinetic nuclear operator, T_e the kinetic electronic operator, V_e the Coulomb potential between electrons, V_{e-N} the Coulomb potential between nuclei and electrons, and V_N the Coulomb potential between nuclei. The total energy of the crystal is denoted by E .

In the BO approximation, which assumes that the electronic cloud reacts instantaneously to the nuclear motion, the wave function solution of Eq. (1) can be approximated as the product

$$\Psi_n^j(\bar{\mathbf{r}}, \bar{\mathbf{R}}) = \chi_n^j(\bar{\mathbf{R}}) \psi_n(\bar{\mathbf{r}}; \bar{\mathbf{R}}), \quad (2)$$

of an electronic part $\psi_n(\bar{\mathbf{r}}; \bar{\mathbf{R}})$, in which $\bar{\mathbf{R}}$ is a parameter, and a nuclear part $\chi_n^j(\bar{\mathbf{R}})$. The electron orbital index is n , and j indexes vibrational states.

The Hamiltonian acting onto the electronic variables is labelled H_{BO} ,

$$H_{BO} = T_e + V_e + V_{e-N} + V_N \quad (3)$$

where V_N is then a constant energy term determined for a given nuclei configuration $\bar{\mathbf{R}}$. Thus H_{BO} is parametrized by $\bar{\mathbf{R}}$. The electronic wave function $\psi_n(\bar{\mathbf{r}}; \bar{\mathbf{R}})$ is solution of the Schrödinger equation,

$$H_{BO} \psi_n(\bar{\mathbf{r}}; \bar{\mathbf{R}}) = \varepsilon_n(\bar{\mathbf{R}}) \psi_n(\bar{\mathbf{r}}; \bar{\mathbf{R}}), \quad (4)$$

which introduces the energy surface $\varepsilon_n(\bar{\mathbf{R}})$. In the BO approximation the lattice dynamics is described by

$$[T_N + \varepsilon_n(\bar{\mathbf{R}})] \chi_n^j(\bar{\mathbf{R}}) = E_n^j \chi_n^j(\bar{\mathbf{R}}) \quad (5)$$

where the vibrational wave functions $\chi_n^j(\bar{\mathbf{R}})$ are the orthonormal solutions and E_n^j is the total energy of the whole crystal. Equations (4) and (5) imply that $\{\psi_n\}$ and $\{\chi_n\}$ are complete basis sets of eigenvectors of H_{BO} and of the nuclear Hamiltonian $[T_N + \varepsilon_n(\bar{\mathbf{R}})]$, respectively, leading to the completeness relations

$$\sum_n \psi_n^*(\bar{\mathbf{r}}, \bar{\mathbf{R}}) \psi_n(\bar{\mathbf{r}}', \bar{\mathbf{R}}) = \delta(\bar{\mathbf{r}} - \bar{\mathbf{r}}'); \forall \bar{\mathbf{R}}, \quad (6)$$

$$\sum_j \chi_n^j(\bar{\mathbf{R}}) \chi_n^j(\bar{\mathbf{R}}') = \delta(\bar{\mathbf{R}} - \bar{\mathbf{R}}'); \forall n. \quad (7)$$

The phonon-induced displacement of nucleus I in the Cartesian direction α

$$u_I^\alpha = R_I^\alpha - R_{I,(\text{eq})}^\alpha \quad (8)$$

is small compared to the atomic bond length. Thus a Taylor expansion of the BO energy surface as a function of the nuclear displacements can be carried out and is truncated at the second order in the harmonic approximation. The energy scale is shifted such as the zero-order term is null and the first-order term vanishes because forces acting on individual nuclei are zero at equilibrium. In this approximation, $[T_N + \varepsilon_n(\bar{\mathbf{R}})]$ becomes the nuclear harmonic Hamiltonian as

$$\mathcal{H} = \sum_{I=1}^N \sum_{\alpha=1}^3 \frac{(P_I^\alpha)^2}{2M_I} + \frac{1}{2} \sum_{I,J}^N \sum_{\alpha,\alpha'}^3 u_I^\alpha \mathcal{C}_{\alpha\alpha'}^{IJ} u_J^{\alpha'}, \quad (9)$$

where T_N is explicitly written in terms of \mathbf{P}_I , the momentum operator of the I th nucleus. In Eq. (9) we have introduced the interatomic force constant matrix \mathcal{C} whose elements are

$$\mathcal{C}_{\alpha\alpha'}^{IJ} = \left. \frac{\partial^2 \varepsilon_n(\bar{\mathbf{R}})}{\partial u_I^\alpha \partial u_J^{\alpha'}} \right|_{(\text{eq})}. \quad (10)$$

Rescaling \mathcal{C} by the nuclei masses define the dynamical matrix, whose diagonalization as

$$\sum_{J=1}^N \sum_{\alpha'=1}^3 \frac{\mathcal{C}_{\alpha\alpha'}^{IJ}}{\sqrt{M_I M_J}} \epsilon_{J\mu}^{\alpha'} = \varpi_\mu^2 \epsilon_{I\mu}^\alpha, \quad (11)$$

provides phonon polarization vectors $\epsilon_{I\mu}^\alpha$ and phonon frequencies ϖ_μ , where μ indexes phonon modes. Using in Eq. (9)

$$u_I^\alpha = \sum_{\mu=1}^{3N} \frac{1}{\sqrt{M_I}} \epsilon_{I\mu}^\alpha q_\mu, \quad (12)$$

$$P_I^\alpha = \sum_{\mu=1}^{3N} \sqrt{M_I} \epsilon_{I\mu}^\alpha p_\mu, \quad (13)$$

which introduce the normal coordinates q_μ and $p_\mu = \dot{q}_\mu$, \mathcal{H} can be written as a sum of $3N$ independent Hamiltonian operators of harmonic oscillators

$$\mathcal{H} = \sum_{\mu=1}^{3N} \frac{1}{2} (p_\mu^2 + \varpi_\mu^2 q_\mu^2). \quad (14)$$

Nevertheless, a harmonic model considers the phonon normal modes as independent quasiparticles and does not account for any anharmonic phenomenon, such as thermal expansion. In this work QHA is used to include thermal expansion effects. The model is no longer purely harmonic but does not describe phonon-phonon interaction, as the phonon normal modes are still independent. Within QHA, the probability $\mathcal{P}(\bar{\mathbf{q}}_\mu)$ of finding the system in any set of normal coordinates $\bar{\mathbf{q}}_\mu$, is expressed

as a product of Gaussian functions following a normal distribution whose widths depend on temperature and phonon frequency.⁵² The Gaussian functions are centered on $q_\mu = 0$, i.e., at the equilibrium position when $\mathbf{u}_I = \mathbf{0}$ (Eq. 12). The $\mathcal{P}(\bar{\mathbf{R}})$ probability distribution is written as

$$\mathcal{P}(\bar{\mathbf{R}}) = \mathcal{A} \exp \left(- \sum_{IJ\alpha\alpha'\mu} \frac{\sqrt{M_I M_J}}{2a_\mu^2} \epsilon_{I\mu}^\alpha \epsilon_{J\mu}^{\alpha'} u_I^\alpha u_J^{\alpha'} \right) \quad (15)$$

with \mathcal{A} a normalization constant. The a_μ normal length of the μ vibration mode is the standard deviation of collective normal coordinates $\bar{\mathbf{q}}$ and depends explicitly on temperature T and phonon frequencies ϖ_μ

$$a_\mu = \sqrt{\frac{\hbar}{2\varpi_\mu} \coth \left(\frac{\beta \hbar \varpi_\mu}{2} \right)}, \quad (16)$$

with $\beta = 1/k_B T$. Equation (16) describes how the phonon normal modes are thermally populated. The statistical average of any observable \mathcal{O} is then

$$\langle \mathcal{O} \rangle = \int d\bar{\mathbf{R}} \mathcal{O}(\bar{\mathbf{R}}) \mathcal{P}(\bar{\mathbf{R}}). \quad (17)$$

For a given crystal, after calculating and diagonalizing the dynamical matrix (Eq. 11) to obtain the phonon frequencies ϖ_μ and polarization vectors ϵ_μ , a set of N_c nuclear configurations obeying the $\mathcal{P}(\bar{\mathbf{R}})$ quantum statistical distribution is generated. For each μ mode, a set $\{x_\mu^i\}_{i=1\dots N_c}$ of N_c random Gaussian numbers is created. Then, each x_μ is multiplied by the corresponding normal length a_μ , as defined in Eq. (16). The set of so-generated normal coordinates $\{q_\mu^i = x_\mu^i a_\mu\}_{i=1\dots N_c}$ obeys the probability distribution (Eq. 15). The nuclear position collective vectors $\{\bar{\mathbf{R}}^i\}_{i=1\dots N_c}$ are obtained using Eqs. (8) and (12) such as

$$R_I^{\alpha,i} = R_{I,(\text{eq})}^{\alpha,i} + \sum_{\mu=1}^{3N} \frac{1}{\sqrt{M_I}} \epsilon_{I\mu}^\alpha a_\mu x_\mu^i. \quad (18)$$

According to the importance sampling technique, Eq. (17) is equivalent to

$$\langle \mathcal{O} \rangle \simeq \frac{1}{N_c} \sum_{i=1}^{N_c} \mathcal{O}(\bar{\mathbf{R}}^i). \quad (19)$$

In this work, $\mathcal{O}(\bar{\mathbf{R}}^i)$ is either the nuclear magnetic shielding tensor, the EFG tensor or the XANES cross section for the i th configuration.

B. Nuclear Magnetic Resonance spectroscopy

To compare with NMR experiments, for each nucleus, the isotropic value of the magnetic shielding tensor σ is evaluated as

$$\sigma_{\text{iso}} = \frac{1}{3} \text{tr}(\sigma). \quad (20)$$

More precisely, the isotropic chemical shift $\delta_{\text{iso}} \simeq -(\sigma_{\text{iso}} - \sigma_{\text{ref}})$ is considered, where σ_{ref} is the isotropic shielding of the standard reference. Unlike the Larmor frequency, δ_{iso} contains the response of the electronic system to the magnetic perturbation and is therefore an explicit function of the electronic environment around the probed nucleus. Thus, $\delta_{\text{iso}} = \delta_{\text{iso}}(\bar{\mathbf{R}})$ and $\langle \delta_{\text{iso}}(\bar{\mathbf{R}}) \rangle$ is obtained as in Eq. (19).

C. XANES spectroscopy

In a single-electron approach, at the K -edge, the XANES cross-section, in the electric dipole approximation is usually given by⁵³

$$\sigma(\hbar\omega) = 4\pi^2\alpha_0\hbar\omega \sum_n |\langle \psi_n | \hat{\mathbf{e}} \cdot \mathbf{r} | \psi_{1s} \rangle|^2 \delta(\varepsilon_n - \varepsilon_{1s} - \hbar\omega). \quad (21)$$

where $\hbar\omega$ and $\hat{\mathbf{e}}$ are the energy and polarization vector of the incident X-ray photon, respectively, and α_0 the fine structure constant. The final $|\psi_n\rangle$ and initial $|\psi_{1s}\rangle$ electronic states of energy ε_n and ε_{1s} , respectively, are solution of Eq. (4).

Equation (21) rests upon the assumption that the nuclei are fixed in a generic configuration, hence σ is parametrized by $\bar{\mathbf{R}}$, i.e., $\sigma(\hbar\omega) = \sigma(\hbar\omega; \bar{\mathbf{R}})$. A more rigorous expression of the cross section accounting for the total system of nuclei and electrons is

$$\sigma_{\text{tot}}(\hbar\omega) = 4\pi^2\alpha_0\hbar\omega \sum_{n,j} |\langle \Psi_n^j | \hat{\mathbf{e}} \cdot \bar{\mathbf{r}} | \Psi_{1s}^0 \rangle|^2 \delta(E_n^j - E_{1s}^0 - \hbar\omega) \quad (22)$$

where the Ψ_{1s}^0 initial state and Ψ_n^j final states are defined as in Eq. (2). In Appendix A, it is demonstrated that σ_{tot} can be expressed, using the first order of the expansion given in Eq. (A3), by

$$\sigma_{\text{tot}}(\hbar\omega) = \int d\bar{\mathbf{R}} \rho(\bar{\mathbf{R}}) \sigma(\hbar\omega; \bar{\mathbf{R}}), \quad (23)$$

with $\rho(\bar{\mathbf{R}})$ the quasi-harmonic weighting displacement distribution. The next orders of the expansion in Eq. (A3) are not considered in the present work. In Eq. (23), σ_{tot} is the average of individual configuration cross sections $\sigma(\hbar\omega; \bar{\mathbf{R}})$ using a probability distribution that takes into account the temperature and vibrations frequencies in a form consistent with Eq. (19).

III. EXPERIMENTAL AND CALCULATION DETAILS

A. Experimental setup

Mg K -edge X-ray absorption experiments were performed at the LUCIA beam line (SOLEIL Saint-Aubin, France).⁵⁴ The incident energy range (1280–1400 eV) was selected to include the Mg K -edge using a double Beryl

monochromator. The pressure in the experimental chamber was 10^{-7} mbar. The incident X-ray beam was set to a spot size of 1×2 mm². Temperature-dependent measurements were conducted at 300 K, 573 K, 773 K, 873 K and 1273 K using a boron nitride furnace. Only the spectra recorded at 300 K, 573 K and 873 K are shown. The 4 cm² MgO single crystal was held using a perforated lamella of molybdenum. The temperature of the sample was measured using a Chromel-Alumel thermocouple. The spectra were recorded in fluorescence mode with a four element Silicon Drift Diode detector, protected from infrared and visible radiations by a thin beryllium window. To maximize the signal/noise ratio, each point was obtained after a 5 second acquisition time and 5 spectra were measured for each temperature. The self-absorption correction and spectra normalization were applied as in Ref. 20.

The temperature-dependent measurements of ²⁵Mg and ¹⁷O static isotropic chemical shifts in MgO are taken from Ref. 11. The NMR active isotopes ²⁵Mg and ¹⁷O have weak natural abundances and gyromagnetic ratios, thus experiments required isotopically enriched samples. Both nuclei are quadrupolar ($I_{\text{spin}} = 5/2$) but, as any atomic site in MgO presents O_h symmetry, the experimental EFG vanishes. Therefore, NMR peaks do not suffer from quadrupolar broadening and shifting.

B. Calculation details

TABLE I. Parameters of generation for Troullier-Martin ultrasoft (US) and norm-conserving (NC) pseudopotentials. Bessel functions are used to pseudize the augmentation charges. The radii are in Bohr units.

Atom	Valence states (Radius)	Local part
Mg (NC)	$3s^1(2.00) 3p^0(2.00) 3d^0(2.00)$	d
O (NC)	$2s^2(1.45) 2p^3(1.45)$	p
Mg ^a (US)	$3s^2(2.50) 3p^0(2.60) 3d^0(2.30)$	d
O (US)	$2s^2(1.35) 2p^4(1.35)$	p

^a The pseudopotential of the absorbing Mg atom was generated using the same parameters but with only one $1s$ core electron and used in the XANES calculation.

All the calculations were performed using the pseudopotential, plane wave QUANTUM ESPRESSO suite of codes,⁵⁵ within the DFT-PBE generalized gradient approximation (GGA).⁵⁶ The details of the pseudopotential used herein are given in Table I. Most of the calculations were done using ultrasoft⁵⁷ GIPAW⁵⁸ pseudopotentials except for the NMR calculations for which norm-conserving Troullier-Martin⁵⁹ GIPAW pseudopotentials were preferred.

The method detailed in Sec. II has been carried out creating the configurations at the Quasi-Harmonic level with the Stochastic Self-Consistent Harmonic Approx-

mation (SSCHA) code^{60,61} starting from the QHA dynamical matrices of MgO, which crystallizes in space group $Fm\bar{3}m$ with a room temperature lattice parameter $a = 4.21$ Å. The NMR and XANES calculations were performed for temperatures ranging from 0 K to 1273 K with the experimental lattice parameters,⁶² so that the configurations and spectroscopic results account for the thermal-expansion anharmonic effect. The 0 K calculations were performed using the 12 K lattice parameter.⁶³

Self-consistent electronic densities were calculated in the unit-cell at the volume of each corresponding temperature. A $4 \times 4 \times 4$ \mathbf{k} -point grid sampled the Brillouin zone,⁶⁴ and a plane-wave energy cutoff (density) for the wave functions of 45 (540) Ry was chosen. Then, the dynamical matrices were calculated using Density-Functional Perturbation Theory^{65,66} on a \mathbf{q} -point grid commensurate with the supercell size needed for NMR and XANES calculations thereafter. Long-range electrostatic interactions were taken into account by calculating Born effective charges and electronic dielectric tensor.⁶⁷

NMR calculations were performed using the GIPAW package.^{58,68} For each temperature, the calculations were conducted for $2 \times 2 \times 2$ supercell configurations containing 64 atoms. Each calculation was done on a $2 \times 2 \times 2$ \mathbf{k} -point grid, with a plane-wave energy cutoff for the wave functions (resp. density) of 90 (resp. 360) Ry. The convergence was reached for ten configurations at each temperature. For a given temperature, 640 isotropic shielding tensors were calculated and averaged for each nucleus. In this work, σ_{ref} is chosen so that experimental and calculated values match at room temperature. The principal components V_{xx} , V_{yy} and V_{zz} of the EFG tensor defined with $|V_{zz}| > |V_{xx}| > |V_{yy}|$ are obtained by diagonalization of the tensor. The quadrupolar coupling constants C_Q defined as $C_Q = eQV_{zz}/h$ were estimated with Q values from Ref. 69 and were found negligible at each temperature. This behavior is consistent with the crystal symmetry and experimental results. Indeed, in a perfect cubic environment we expect the first-order EFG tensor quantities to vanish.

For each temperature, the XANES spectra were calculated using the XSpectra package^{70,71} in $3 \times 3 \times 3$ supercell configurations containing 216 atoms, each including one $1s$ full core-hole in a random Mg site. The self-consistent electronic density was obtained at the Γ point of the Brillouin zone with a plane-wave energy (resp. density) cutoff of 45 (resp. 540) Ry. The XANES theoretical spectra were performed on a $4 \times 4 \times 4$ \mathbf{k} -point grid with a constant broadening parameter of 0.5 eV. For a given configuration, three polarized XANES spectra were calculated for the X-ray polarization vector $\hat{\mathbf{e}}$ parallel to each of the Cartesian axes and the average gave an isotropic XANES spectrum. As a convergence criterium, it has been verified that the averaged polarized spectra along each Cartesian direction matched, as expected in a cubic crystal. The convergence was reached for a number of 30 configurations at each temperature. In the pseudopotential approximation, only valence-electrons are consid-

ered, hence the energy scale has no physical meaning and a core-level shift has to be applied before comparing and averaging theoretical spectra (Eq. 19). Similarly to previous works,^{72–74} the core-level shift in the i th configuration is taken into account as follows:

$$E \rightarrow E - \varepsilon_{\text{LUB}}^i + (E_{\text{XCH}}^i - E_{\text{GS}}^i). \quad (24)$$

In this rescaling, the energy of the lowest unoccupied electronic band $\varepsilon_{\text{LUB}}^i$ was subtracted and the energy difference between the system with one $1s$ core-hole and one electron in the first available electronic state (E_{XCH}^i) and that of the ground state (E_{GS}^i) was added. Finally, all the spectra were shifted by 1303.8 eV to match the experimental main edge peak energy position at room temperature. To interpret XANES spectra, local and partial density of states (DOS) were calculated in the $3 \times 3 \times 3$ supercell configurations using Löwdin projections on a $4 \times 4 \times 4$ \mathbf{k} -point grid with a Gaussian broadening parameter of 0.3 eV.

IV. RESULTS AND DISCUSSION

A. Solid-state NMR spectroscopy

Figure 1 compares the temperature-dependence of the experimental NMR measurements from Ref. 11 with the calculated isotropic chemical shifts δ_{iso} of ^{25}Mg and ^{17}O in MgO up to 1273 K. For both nuclei, the calculated values closely reproduce the experimental trend: the chemical shift increases with temperature. In addition, the contribution of the thermal expansion is displayed. The incorporation of the quantum motion of nuclei is mandatory, since it improves the agreement with experiment, especially for ^{25}Mg . Without the quantum motion, considering only the thermal expansion leads to a downward trend in ^{25}Mg and an upward one in ^{17}O . These opposite trends come from the fact that unlike ^{25}Mg , the chemical shift of ^{17}O is not a function of the Mg-O bond length. Indeed, the chemical shift of ^{17}O depends on the interaction between the empty d states of ^{25}Mg and the $2p$ states of ^{17}O , which results in a deshielding of ^{17}O .⁷⁵

TABLE II. Slopes of the temperature-dependent chemical shifts δ_{iso} for temperatures ranging from 300 K to 1300 K, in ppm.K⁻¹. The given values are the best fit lines in the room-to-high temperature region. The experimental results are reported and compared to calculated values from this work and previous studies.

Nucleus	Expt. ^a	This work	Calc. ^b	Calc. ^c
^{25}Mg	0.002	0.003	0.004	0.005
^{17}O	0.008	0.010	0.011	0.005

^a Ref. 11

^b Ref. 41

^c Ref. 42

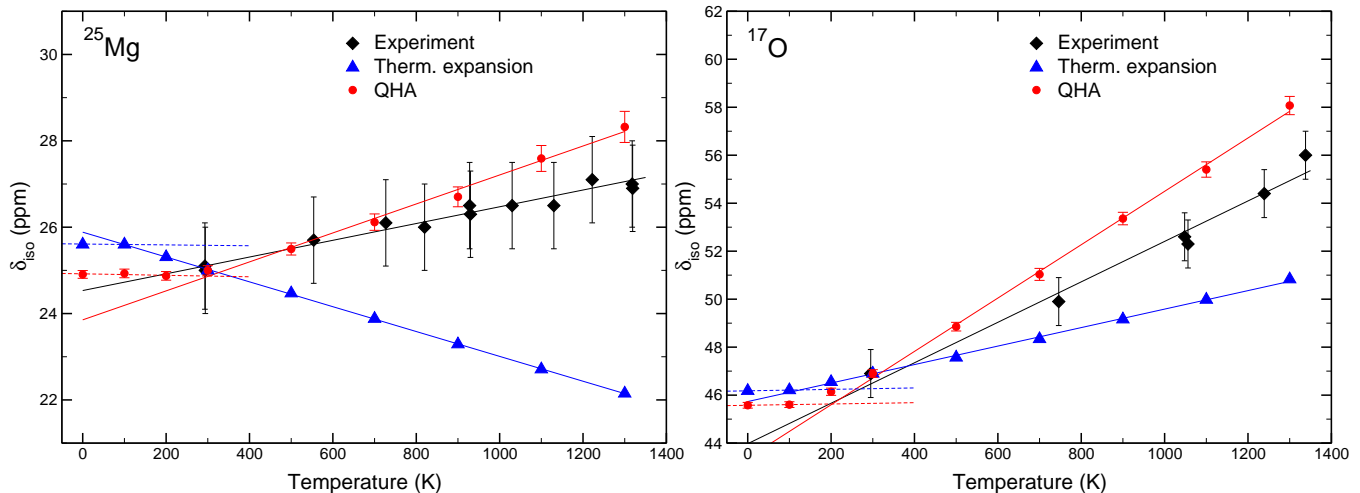


FIG. 1. (Color online) Temperature-dependent isotropic chemical shift of ^{25}Mg and ^{17}O in MgO obtained experimentally¹¹ (diamonds), calculated in the QHA (circles), and considering only the thermal expansion (triangles). The linear fits of each dataset are displayed. For the QHA calculation, two independent linear contributions are observed: from 0 K to 100 K and from 300 K to 1273 K. The experimental errors bars are set to ± 1 ppm as in the original paper, while the calculated error bars are the statistical uncertainties.

The linear trend behavior of the chemical shift observed from 300 K to 1273 K is consistent with experiments and previous theoretical studies.^{41,42} Our results show a better agreement with experiments than other theoretical studies, the corresponding slopes obtained for each nucleus are summarized in Table II. The method used in Ref. 41 is similar to ours, but the remaining discrepancies may come from a less accurate description of the phonons dispersion and quasi-harmonic vibrational wave functions. In Ref. 42, the coupling between the phonons and the chemical shift tensor was expanded in terms of vibrational-mode amplitudes and was assumed to be quadratic. However, in this study, the thermal expansion was neglected, thus, the results cannot be compared to experiment and the same slope is reported for the temperature-dependence of both nuclei unlike experiments.

The linear behavior in the room-to-high temperature region arises from a combination of both the thermal expansion and dynamics of nuclei. These two effects are constant in the low-temperature regime, from 0 K to 100 K, where the vanishing thermal expansion gives rise to a flat temperature dependence and the dynamics of the nuclei reduces to a $\Delta\delta_{\text{iso}}$ constant term (Fig. 1). The zero-point renormalization of the chemical shift is evaluated to $\Delta\delta_{\text{iso}}(^{25}\text{Mg}) = 0.69$ ppm and $\Delta\delta_{\text{iso}}(^{17}\text{O}) = 0.60$ ppm, respectively. Above 300 K, the amplitude of the dynamical part outweighs the thermal expansion. Finally, in the intermediate temperature region (typically between 100 K and 300 K) there is a competition between the two components of the temperature-dependence that leads to the observed curvature.

The origin of the remaining discrepancies between calculated and experimental slopes has to be investigated.

The overestimation of the temperature-dependence of both nuclei chemical shifts could be related to a deficiency of GGA. Indeed, it is well known that GGA overestimates slightly the interatomic distances of solids and underrates phonon frequencies.⁷⁶ Although experimental lattice parameters are chosen to balance this effect, the use of more accurate GGA functionals^{77,78} might enhance the agreement. Furthermore, it has been noticed that, in ionic compounds containing alkaline-earth cations, the calculation-experiment correlation lines of NMR parameters, as calculated within GGA, deviate from the 1 ideal value.⁷⁹ In the case of CaO, it has been observed that the shortening of the bond length induces an artificial hybridization between the $3d$ states of Ca and the $2p$ of O.⁷⁵ This problem was addressed by the use of a corrected Ca pseudopotential. To a lesser extent this problem can occur in MgO. Laskowski *et al.*⁷⁹ proposed to use GGA+ U instead of standard GGA to better describe the $3d$ states of the cation. Finally, one may argue of a failure of QHA, but the theory has revealed to accurately provide the lattice dynamical properties in MgO up to 1100 K under ambient pressure conditions.⁸⁰ To go beyond QHA, anharmonic effects in periodic solids can be investigated in a numerically feasible manner using the vibrational self-consistent field method⁸¹ or the SSCHA.⁶¹

B. XANES spectroscopy

In Fig. 2(a) the experimental Mg K -edge XANES spectra are reported. While temperature continuously smoothes the XANES features, the P pre-edge peak increases and shifts towards lower energy. To a lesser

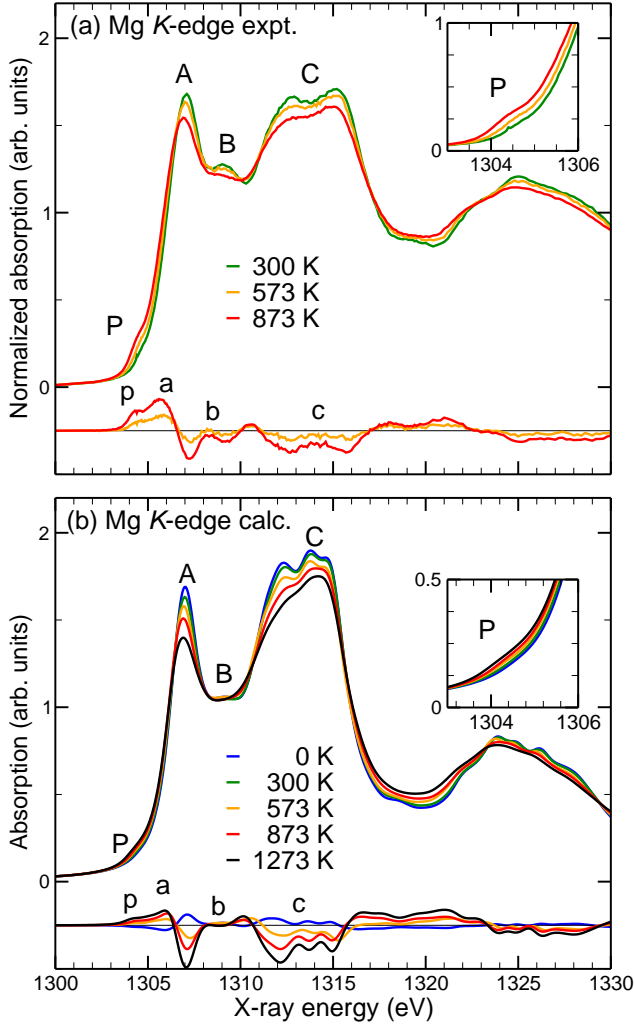


FIG. 2. (Color online) Mg *K*-edge XANES experimental (a) and QHA-calculated (b) spectra of MgO, for temperature up to 1273 K, along with difference of each spectrum with respect to the room-temperature one.

extent, this energy shift is also visible for the A main edge peak and the following features. These temperature effects have been also observed at the Al *K*-edge in corundum (α - Al_2O_3) and beryl ($\text{Be}_3\text{Al}_2\text{Si}_6\text{O}_{18}$).²⁰ The corresponding calculated XANES spectra are plotted in Fig. 2(b) along with the 0 K and 1273 K spectra. Calculations reproduce closely experiments over all the explored incident X-ray photon energy range, as highlighted by the similarity of the difference of each spectrum with the room-temperature one. However, the intensity of the calculated pre-edge is underestimated: the experimental and calculated P/A intensity ratios are about 1/5 and 1/7, respectively. This mismatch may come from the first-order expansion of the X-ray absorption cross section (Eq. 23). Going further than the first-order is a possible improvement of the method. In addition, as for NMR, configurations obtained beyond QHA could lead

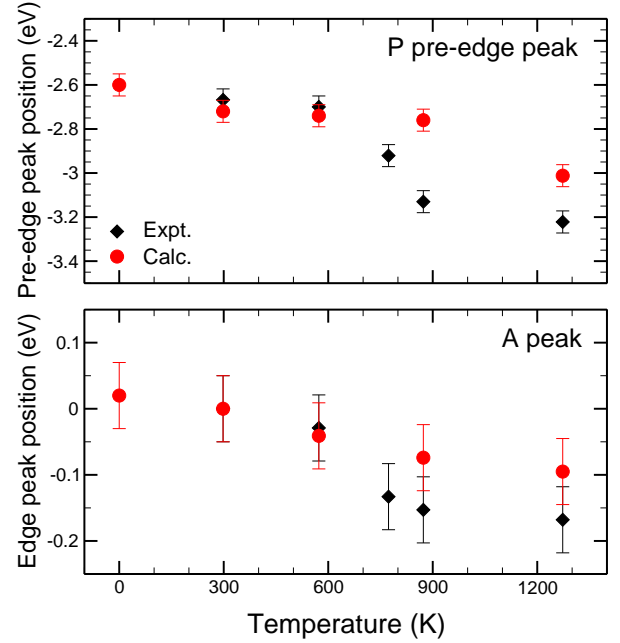


FIG. 3. (Color online) Experimental and calculated energy positions of P (upper panel) and A (lower panel) peaks as a function of temperature. The energy positions are given with respect to the A peak position at 300 K.

to a better agreement with experiment.^{60,81}

The temperature-dependence of the P and A peaks energy positions is showed in Fig. 3. For temperature ranging from 300 K to 1273 K, the theory-experiment agreement is satisfactory: the experimental and calculated P peak variation is 0.55 eV and 0.41 eV, respectively. For peak A, the experimental (resp. calculated) variation is 0.17 eV (resp. 0.12 eV). The results are comforted by the experimental observations at the Al *K*-edge in corundum where the pre-edge position decreased of about 0.4 eV from 300 K to 930 K.²⁰ The origin of these shifts may be related to the band gap evolution in temperature. In ionic compounds, the lattice expansion affects electronic bands. In MgO, the band gap was shown to decrease by 0.91 eV, from 300 K to 1273 K, using optical reflectivity measurements.⁸² Moreover, the electron-phonon interaction contributes more than the thermal expansion to the band gap narrowing.^{83,84} Over the same range of temperature, our calculations achieved a similar band gap decrease (0.78 eV), while the decrease only due to thermal expansion is 0.3 eV.

The energy shift to lower energy does not exclusively concern the P and A features since it is visible over all the spectral energy range. For instance, peak D moves of about 0.1 eV to lower energy as temperature increases. The decreasing shift agrees with the empirical Natoli's rule ($Ed^2 = \text{cste}$),⁸⁵ which states that the energy position decreases with increasing interatomic distance. Therefore, this signature can be related to the thermal expansion. Figure 4 displays the Mg *K*-edge XANES spectra

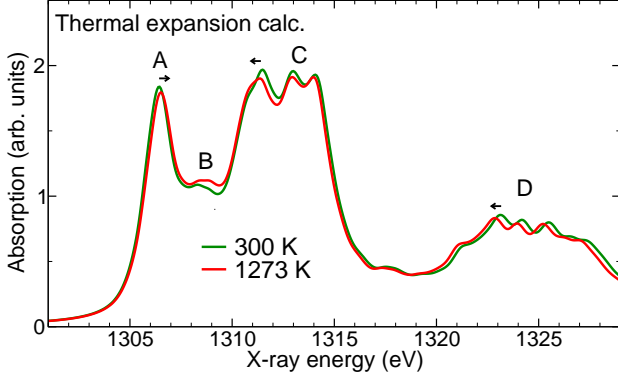


FIG. 4. (Color online) Calculated Mg *K*-edge XANES spectra in MgO considering only the thermal expansion.

calculated in the equilibrium configuration at the volumes corresponding to 300 K and 1273 K. The 1273 K spectrum is more contracted than the 300 K spectrum. The C and D features move down toward lower energy with increasing interatomic distance as observed experimentally. On the contrary, in opposite trend with experiment, peak A shifts toward higher energy. Therefore, thermal expansion does not fully explain the shifting trends, especially at lower energy, where vibrations are mandatory to reproduce the correct spectral-feature positions.

Former studies already proposed that the P peak originates from the vibration-induced violation of the dipole forbidden $1s \rightarrow 3s$ transitions.^{20–22} To further analyze the P peak origin, Fig. 5 compares the theoretical XANES spectra obtained at 0 K, by including or not the zero-point motion. In addition, Fig. 5 displays all the core-level shifted individual configuration spectra in the background. The phonon influence on the XANES spectra is characterized by two main features. First, similarly to a convolution and in agreement with the theoretical framework of Fujikawa,²⁶ the inclusion of the 0 K quantum fluctuations globally smoothes the XANES spectrum. Second, the zero-point motion induces a pre-edge peak that is totally absent in the equilibrium spectrum, i.e., when the atoms are fixed at their equilibrium positions. Hence, Fig. 5 highlights the quantum origin of the pre-edge. Moreover, the weak difference in the pre-edge intensities between 0 K and 300 K calculations emphasizes the prominent role of quantum effects up to room temperature [Fig. 2(b)]. A better description of the P and A peaks intensities and variations could be achieved by the phonon-renormalization of the electronic energies directly in the self-consistent calculation, as performed in Refs. 86–89.

The 0 K individual configuration spectra present a strong dispersion around the averaged spectrum (Fig. 5). This dispersion increases with temperature. Some of the individual configuration spectra exhibit a strong P peak while some other do not, whatever the temperature. Two

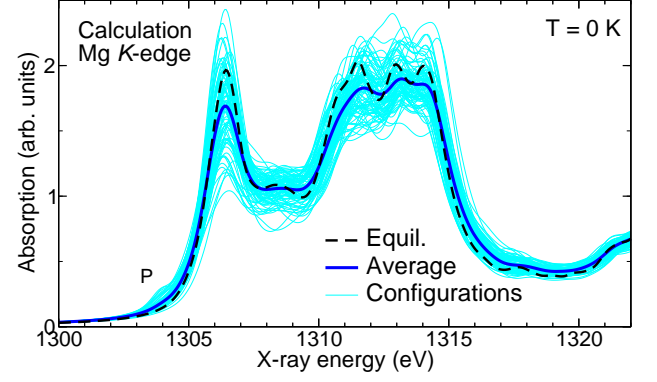


FIG. 5. (Color online) Impact of the zero-point motion on the theoretical Mg *K*-edge XANES spectrum of MgO. The dashed spectrum is obtained with the atoms fixed at their equilibrium positions in the 12 K experimental volume.⁶³ The solid spectrum is the average of the 30 configuration spectra (in light blue).

individual configuration XANES spectra at $T = 1273$ K, one with a pre-edge and one without, have been selected and analyzed using local and partial DOS [Figs. 6(b,c)]. For comparison, Fig. 6(a) displays the case of the standard calculation with atoms fixed at their equilibrium positions at $T = 1273$ K. The partial and local DOS plotted in Fig. 6 are the *s* and *p* empty DOS projected on (i) the absorbing Mg, (ii) the first O neighbors, (iii) the next Mg neighbors, and (iv) the next O neighbors. Whatever the configuration, the core-hole strongly modifies the *s* and *p* empty states of Mg, leading to two rather localized peaks, which coincide with P and A, respectively. P is only visible if *sp* hybridization of the Mg absorbing states occurs [Figs. 6(c)]. This *sp* mixing of the Mg absorbing states also induces a stronger *p* DOS of oxygen. The *sp* hybridization due to the dynamical distortion of the MgO_6 octahedron does not systematically occur [Fig. 6(b)]. The contribution of the lowest unoccupied band to the electronic charge density ($\pm |\psi_{\text{LUB}}|^2$) gives a representation of the electronic state probed in the P peak and enlightens the effect of the MgO_6 octahedron distortion. In the equilibrium configuration [Fig. 6(a)] the isosurface shows a centrosymmetric cubic shape. The distortion of the lattice strongly impacts $\pm |\psi_{\text{LUB}}|^2$ [Fig. 6(b)], however, it is not sufficient to create a pre-edge peak. The P peak emerges if the distortion of the MgO_6 octahedron induces a *p*-like character on the neighboring O atoms, as already observed in the DOS [Fig. 6(c)]. To conclude, the breakdown of the symmetry is mandatory to induce the *sp* hybridization and the forbidden $1s \rightarrow 3s$ transition but is not sufficient.

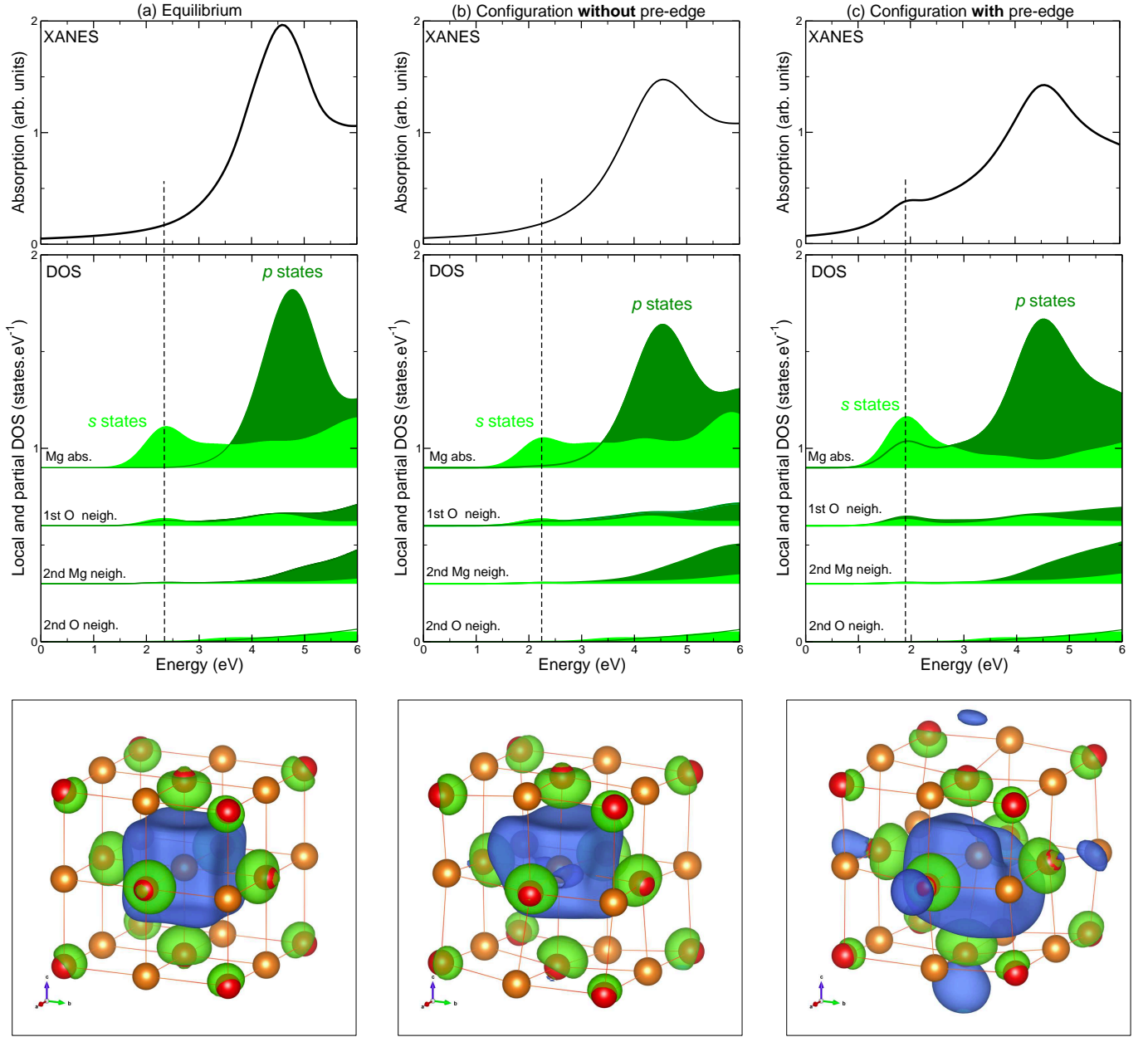


FIG. 6. (Color online) Pre-edge peak analysis. Three configurations at 1273 K are considered: the equilibrium structure (a), an individual configuration not leading to pre-edge peak (b) and an individual configuration that leads to pre-edge peak (c). Top panel: Mg K -edge theoretical XANES spectra. Middle panel: local and partial electronic density of states (see text for details). Bottom panel: isosurfaces of $\text{sign}(\psi_{\text{LUB}})|\psi_{\text{LUB}}|^2$, where ψ_{LUB} is the electronic wave function of the lowest unoccupied band, whose energy is indicated by the vertical dashed line in top and middle panels (negative and positive signs are colored in green and blue, respectively). The Mg atoms are displayed in orange and O atoms in red. The pictures are centered on the absorbing Mg atom. The isosurface level is set to $6 \times 10^{-4} a_0^{-3}$, with a_0 the Bohr radius.

V. CONCLUSION

A DFT-based approach enabling to successfully introduce quasi-harmonic quantum thermal fluctuations of nuclei in NMR and XANES spectroscopies has been presented. This method, avoiding the explicit calculation of the electron-phonon coupling parameters, provides an

efficient framework to analyze phonon effects occurring in both spectroscopies. The calculated spectral data obtained in the MgO proof-of-principle compound are in good agreement with experimental datasets, which supports the reliability of our approach.

The combination of experiments and first-principle calculations have enabled to investigate the influence of the

quantum vibrations in both spectroscopies. A similar behavior is revealed: the zero-point phonon renormalization of NMR and XANES spectra improves the experiment-calculation agreement and therefore could be used on a regular basis to reproduce experimental data even at low temperatures.

In NMR, the experiment-calculation agreement is improved with respect to previous theoretical studies. The temperature-dependence of the chemical shifts results from both contributions of thermal expansion and nuclear dynamics, and reduces to a constant renormalization term at low temperature.

In the case of XANES, the temperature-dependence of XANES features is reproduced over a large range of temperatures. An analytic expression of the phonon-dependent X-ray absorption cross section is derived at the first order of the electronic Green's function expansion. It appears that keeping only the first term in the expansion of Eq. (A3) is a suitable approximation to calculate XANES spectra at finite temperature. It appears that the first-order calculation of XANES spectra at finite temperature is a suitable approximation. Nevertheless, the implementation of the higher-orders correction terms could improve the pre-edge intensity modeling. The presence of the pre-edge feature is a relevant signature of phonon effects. A thorough study of the mechanism from which the pre-edge emerges is conducted. The breakdown of the coordination symmetry is mandatory to induce the pre-edge and a *p*-like character arises on the neighboring O atoms if the pre-edge feature is discernible. The pre-edge energy variation in temperature is related to the band gap temperature-dependence, whereas the variation of the high-energy structures originates from the thermal expansion.

The results obtained for MgO can be extrapolated to other light-element oxides. In the case of XANES spectroscopy, the method is applied to corundum in a forthcoming publication.⁹⁰ Techniques closely related to XANES, such as Non Resonant Inelastic X-ray Scattering and core-loss Electron Energy Loss Spectroscopy, may also be affected by vibrations and could highly benefit from this theoretical framework.

ACKNOWLEDGMENTS

This work was supported by French state funds managed by the ANR within the Investissements d'Avenir programme under reference ANR-11-IDEX-0004-02, and more specifically within the framework of the Cluster of Excellence MATISSE led by Sorbonne Universités. It was performed using the HPC resources of GENCI-IDRIS (grants: 2015-100172). Experiments were performed on the LUCIA beam line at SOLEIL Synchrotron (proposal: 20141057). The authors acknowledge Guillaume Radtke, Étienne Balan, Delphine Vantelon, Jean-Paul Itié and Yves Joly for very fruitful discussions and Lorenzo Paulatto for his help with the SSCHA code.

Appendix A: Phonon-renormalized X-ray absorption cross-section

In this section we discuss two questions that are rarely addressed in the literature. To describe the first question recall that, in optical spectroscopy of molecules, the equilibrium nuclear positions of the initial and final states of the absorption process are different. This leads to vibronic effects that are often calculated by using the Franck-Condon principle. In X-ray absorption spectroscopy, the experimental spectrum is well reproduced although the final states are calculated for the same nuclear positions as the initial state. How can this be?

The second question has to do with the effect of temperature on X-ray absorption spectra. This effect is often calculated by averaging spectra calculated over a distribution of atomic positions corresponding to the temperature.³³⁻³⁶ In principle, this procedure is not correct although it gives reasonable results in practice. How can this be?

In the present section, we answer these two questions by showing that the usual calculation methods amount to neglecting the nuclear kinetic energy in the absorption process and we show how it is possible to go beyond this approximation.

To describe the effect of nuclear vibrations on XANES spectra, we write the electric dipole absorption cross-section in terms of the wave functions $|\Psi_n^j\rangle$ involving both the electronic and the nuclear variables:

$$\begin{aligned}\sigma_{tot}(\hbar\omega) &= 4\pi^2\alpha_0\hbar\omega \sum_{n,j} |\langle\Psi_n^j|\mathcal{T}|\Psi_0^0\rangle|^2 \delta(E_n^j - E_0^0 - \hbar\omega) \\ &= -4\pi\alpha_0\hbar\omega \langle\Psi_0^0|\mathcal{T}^\dagger \text{Im}G(E_0^0 + \hbar\omega)\mathcal{T}|\Psi_0^0\rangle, \quad (\text{A1})\end{aligned}$$

where we used:⁹¹

$$\sum_n |\Psi_n^j\rangle \delta(E_n^j - E_0^0 - \hbar\omega) \langle\Psi_n^j| = -\frac{1}{\pi} \text{Im} [G(E_0^0 + \hbar\omega)].$$

Equation (A1) is equivalent to Eq. (22) for the transition operator $\mathcal{T} = \hat{\mathbf{e}} \cdot \bar{\mathbf{r}} = \sum_i^{N_e} \hat{\mathbf{e}} \cdot \mathbf{r}_i$. The Green function G of the full electronic and nuclear Hamiltonian is the solution of the following equation

$$[z - H_{BO} - T_N]G(z) = 1, \quad (\text{A2})$$

with the complex energy $z = E + i\gamma$, where γ an infinitesimal positive number or a finite number representing the broadening due to core-hole lifetime and experimental resolution. A straightforward expansion in Eq. (A2) gives

$$G(z) = G_0(z) + G_0(z)T_N G(z), \quad (\text{A3})$$

where $G_0(z) = [z - H_{BO}]^{-1}$ is the Green function in the Born-Oppenheimer approximation. Equation (A3) can be expanded into

$$G(z) = G_0(z) + G_0(z)T_N G_0(z) + \dots \quad (\text{A4})$$

The resolution of X-ray absorption spectra is determined by the lifetime of the core hole (0.36 eV for the *K*-edge

of Mg⁹²). It may be considered that the core hole lifetime will smooth out effects that involve a much smaller energy. Since the nuclear kinetic energy, evaluated using the zero-point energy values,⁹³ is 0.02 eV, it seems reasonable to neglect the kinetic energy T_N and to keep only the first term of the expansion:

$$G(z) \approx G_0(z). \quad (\text{A5})$$

The second term is expected to play a role in the presence of forbidden transitions, but this effect will not be considered in the present paper. We reach the approximate absorption cross-section

$$\sigma_{tot}(\hbar\omega) = -4\pi\alpha_0\hbar\omega \text{Im} \langle \Psi_0^0 | \mathcal{T}^\dagger G_0 \mathcal{T} | \Psi_0^0 \rangle. \quad (\text{A6})$$

In this approximation, the calculation of the phonon-renormalized XANES cross section requires only the Born-Oppenheimer Green function G_0 , for which we now give the following convenient expression:

$$\langle \bar{\mathbf{r}}', \bar{\mathbf{R}}' | G_0 | \bar{\mathbf{r}}, \bar{\mathbf{R}} \rangle = \sum_{n,j} \frac{\langle \bar{\mathbf{r}}', \bar{\mathbf{R}}' | \Psi_n^j \rangle \langle \Psi_n^j | \bar{\mathbf{r}}, \bar{\mathbf{R}} \rangle}{z - \varepsilon_n(\bar{\mathbf{R}})}. \quad (\text{A7})$$

The validity of this expression can be established by showing that it solves the equation for G_0 :

$$[z - H_{BO}] \langle \bar{\mathbf{r}}', \bar{\mathbf{R}}' | G_0 | \bar{\mathbf{r}}, \bar{\mathbf{R}} \rangle = \delta(\bar{\mathbf{R}}' - \bar{\mathbf{R}}) \delta(\bar{\mathbf{r}}' - \bar{\mathbf{r}}). \quad (\text{A8})$$

Equation (A6) is now evaluated as follows

$$\begin{aligned} \sigma_{tot}(\hbar\omega) = & -4\pi\alpha_0\hbar\omega \int d\bar{\mathbf{r}} d\bar{\mathbf{r}}' d\bar{\mathbf{R}} d\bar{\mathbf{R}}' \text{Im} \langle \Psi_0^0 | \mathcal{T}^\dagger | \bar{\mathbf{r}}', \bar{\mathbf{R}}' \rangle \\ & \times \langle \bar{\mathbf{r}}', \bar{\mathbf{R}}' | G_0 | \bar{\mathbf{r}}, \bar{\mathbf{R}} \rangle \langle \bar{\mathbf{r}}, \bar{\mathbf{R}} | \mathcal{T} | \Psi_0^0 \rangle. \end{aligned} \quad (\text{A9})$$

This expression can be simplified by noticing that, in the Born-Oppenheimer approximation, G_0 is diagonal in the nuclear variables. Indeed, by writing the initial and final states in the Born-Oppenheimer approximation (Eq. 2) we obtain

$$\begin{aligned} \langle \bar{\mathbf{r}}', \bar{\mathbf{R}}' | G_0 | \bar{\mathbf{r}}, \bar{\mathbf{R}} \rangle = & \sum_n \frac{\psi_n^*(\bar{\mathbf{r}}'; \bar{\mathbf{R}}') \psi_n(\bar{\mathbf{r}}; \bar{\mathbf{R}})}{z - \varepsilon_n(\bar{\mathbf{R}})} \\ & \times \sum_j \chi_n^{j*}(\bar{\mathbf{R}}') \chi_n^j(\bar{\mathbf{R}}). \end{aligned} \quad (\text{A10})$$

The completeness relation of Eq. (7) turns Eq. (A10) into

$$\begin{aligned} \langle \bar{\mathbf{r}}', \bar{\mathbf{R}}' | g_0 | \bar{\mathbf{r}}, \bar{\mathbf{R}} \rangle = & \delta(\bar{\mathbf{R}} - \bar{\mathbf{R}}') \sum_n \frac{\psi_n^*(\bar{\mathbf{r}}'; \bar{\mathbf{R}}) \psi_n(\bar{\mathbf{r}}; \bar{\mathbf{R}})}{z - \varepsilon_n(\bar{\mathbf{R}})}, \\ = & \delta(\bar{\mathbf{R}} - \bar{\mathbf{R}}') \langle \bar{\mathbf{r}}' | g_0(\bar{\mathbf{R}}) | \bar{\mathbf{r}} \rangle, \end{aligned} \quad (\text{A11})$$

where $g_0(\bar{\mathbf{R}})$ is the electronic Green function for a system where the nuclei are fixed at position $\bar{\mathbf{R}}$. In other words, $g_0(\bar{\mathbf{R}})$ is the solution of

$$(z - H_{BO}) \langle \bar{\mathbf{r}}' | g_0(\bar{\mathbf{R}}) | \bar{\mathbf{r}} \rangle = \delta(\bar{\mathbf{r}}' - \bar{\mathbf{r}}), \quad (\text{A12})$$

where H_{BO} is evaluated at the nuclear positions $\bar{\mathbf{R}}$. Introducing Eq. (A11) in Eq. (A6) the absorption cross-section at the first-order in G_0 is obtained:

$$\begin{aligned} \sigma_{tot}(\hbar\omega) = & -4\pi\alpha_0\hbar\omega \int d\bar{\mathbf{r}} d\bar{\mathbf{r}}' d\bar{\mathbf{R}} \text{Im} \langle \Psi_0^0 | \mathcal{T}^\dagger | \bar{\mathbf{r}}', \bar{\mathbf{R}} \rangle \\ & \times \langle \bar{\mathbf{r}}' | g_0(\bar{\mathbf{R}}) | \bar{\mathbf{r}} \rangle \langle \bar{\mathbf{r}}, \bar{\mathbf{R}} | \mathcal{T} | \Psi_0^0 \rangle. \end{aligned} \quad (\text{A13})$$

The result of Eq. (A13) implies that the XANES calculation requires only the energy surface – nuclear configuration – of the initial state. Hence, Eq. (A13) justifies the use of the ground-state crystallographic structure in the initial (without core-hole) and final (with core-hole) states when calculating the XANES cross-section. The total wave functions can be expressed in the BO approximation (Eq. 2)

$$\begin{aligned} \sigma_{tot}(\hbar\omega) = & -4\pi\alpha_0\hbar\omega \text{Im} \int d\bar{\mathbf{R}} |\chi_0^0(\bar{\mathbf{R}})|^2 \\ & \times \int d\bar{\mathbf{r}} d\bar{\mathbf{r}}' \psi_0(\bar{\mathbf{r}}', \bar{\mathbf{R}}) \hat{\mathbf{e}}^* \cdot \bar{\mathbf{r}}' g_0(\bar{\mathbf{R}}) \hat{\mathbf{e}} \cdot \bar{\mathbf{r}} \psi_0(\bar{\mathbf{r}}, \bar{\mathbf{R}}). \end{aligned} \quad (\text{A14})$$

Equation (A14) proves that the effect of thermal vibrations on XANES spectra can be obtained by averaging individual XANES spectra for nuclear positions $\bar{\mathbf{R}}$ weighted by the distribution function $|\chi_0^0(\bar{\mathbf{R}})|^2$ computed from the ground vibrational mode in the ground state.

However, Eq. (A14) is expressed in a many-body framework, whereas K -edge XANES spectra are usually calculated in a single-electron framework. Since this reduction is a classical problem, we just give a sketch of the derivation. If we rewrite Eq. (A14) in terms of wave functions, we have to deal with matrix elements such as $\langle \psi_n | \hat{\mathbf{e}} \cdot \bar{\mathbf{r}} | \psi_0 \rangle$, where $|\psi_0\rangle$ and $|\psi_n\rangle$ are N_e -body wave functions. If we assume that these wave functions can be expressed as Slater determinants, the fact that $\hat{\mathbf{e}} \cdot \bar{\mathbf{r}}$ is a single-body transition operator implies.⁹⁴

$$\langle \psi_n | \hat{\mathbf{e}} \cdot \bar{\mathbf{r}} | \psi_0 \rangle = \int d\mathbf{r} \phi_{\beta'}^*(\mathbf{r}) \hat{\mathbf{e}} \cdot \mathbf{r} \phi_{\beta}(\mathbf{r}), \quad (\text{A15})$$

where $(\phi_{\beta}, \phi_{\beta'})$ is the only pair of one-electron orbitals that are different in $|\psi_0\rangle$ and $|\psi_n\rangle$, where ϕ_{β} is occupied in $|\psi_0\rangle$ and $\phi_{\beta'}$ in $|\psi_n\rangle$. For a K -edge the resulting expression is

$$\begin{aligned} \sigma_{tot}(\hbar\omega) = & -4\pi\alpha_0\hbar\omega \text{Im} \int d\bar{\mathbf{R}} |\chi_0^0(\bar{\mathbf{R}})|^2 \\ & \times \int d\mathbf{r} d\mathbf{r}' \phi_{1s}(\mathbf{r}', \bar{\mathbf{R}}) \hat{\mathbf{e}}^* \cdot \mathbf{r}' g(\mathbf{r}', \mathbf{r}; \bar{\mathbf{R}}) \hat{\mathbf{e}} \cdot \mathbf{r} \phi_{1s}(\mathbf{r}, \bar{\mathbf{R}}), \end{aligned} \quad (\text{A16})$$

where $g(\mathbf{r}', \mathbf{r}; \bar{\mathbf{R}}) = \sum_{\beta'} \phi_{\beta'}^*(\mathbf{r}'; \bar{\mathbf{R}}) \phi_{\beta'}(\mathbf{r}; \bar{\mathbf{R}}) / (z - e_{\beta'})$. A similar expression can be obtained from more sophisticated many-body perturbation theory.

Considering the cross section in a given nuclear configuration from Eq. (21) gives

$$\sigma_{tot}(\hbar\omega) = \int d\bar{\mathbf{R}} |\chi_0^0(\bar{\mathbf{R}})|^2 \sigma(\hbar\omega; \bar{\mathbf{R}}) \quad (\text{A17})$$

and we demonstrate, restricting ourselves to the first order in the expansion of $G(z)$, that to account for the nuclear motion in the XANES cross section one must average the individual configuration spectra using a probability distribution, which is consistent with Eq. (19). We

used a ground-state phonon wave function $\chi_0^0(\mathbf{R})$ for notational convenience. The generalization to a Boltzmann distribution $\rho(\mathbf{R})$ of phonon states at finite temperature is straightforward and amounts to replacing $|\chi_0^0(\mathbf{R})|^2$ by $\rho(\mathbf{R})$ in Eq. (A17).

* ruidy.nemausat@impmc.upmc.fr

- ¹ G. S. Henderson, F. M. F. de Groot, and B. J. A. Moulton, *Rev. Mineral. Geochemistry* **78**, 75 (2014).
- ² K. Mackenzie and M. Smith, *Pergamon Mater. Ser.*, Pergamon Materials Series, Vol. 6 (Elsevier, 2002).
- ³ A. Vjunov, J. L. Fulton, T. Huthwelker, S. Pin, D. Mei, G. K. Schenter, N. Govind, D. M. Camaioni, J. Z. Hu, and J. A. Lercher, *J. Am. Chem. Soc.* **136**, 8296 (2014).
- ⁴ S. E. Ashbrook and S. Sneddon, *J. Am. Chem. Soc.* **136**, 15440 (2014).
- ⁵ E. Salager, R. S. Stein, S. Steuernagel, A. Lesage, B. Elena, and L. Emsley, *Chem. Phys. Lett.* **469**, 336 (2009).
- ⁶ C. J. Milne, T. J. Penfold, and M. Chergui, *Coord. Chem. Rev.* **277-278**, 44 (2014).
- ⁷ A. Koide, T. Fujikawa, and N. Ichikuni, *J. Electron Spectros. Relat. Phenomena* **195**, 375 (2014).
- ⁸ J. J. Rehr and A. L. Ankudinov, *Coord. Chem. Rev.* **249**, 131 (2005).
- ⁹ T. Charpentier, *Solid State Nucl. Magn. Reson.* **40**, 1 (2011).
- ¹⁰ C. Bonhomme, C. Gervais, F. Babonneau, C. Coelho, F. Pourpoint, T. Azaïs, S. E. Ashbrook, J. M. Griffin, J. R. Yates, F. Mauri, and C. J. Pickard, *Chem. Rev.* **112**, 5733 (2012).
- ¹¹ P. S. Fiske, J. F. Stebbins, and I. Farnan, *Phys. Chem. Mineral* **20**, 587 (1994).
- ¹² A. L. Webber, B. Elena, J. M. Griffin, J. R. Yates, T. N. Pham, F. Mauri, C. J. Pickard, A. M. Gil, R. Stein, A. Lesage, L. Emsley, and S. P. Brown, *Phys. Chem. Chem. Phys.* **12**, 6970 (2010).
- ¹³ M. Chan-Huot, S. Wimperis, C. Gervais, G. Bodenhausen, and L. Duma, *ChemPhysChem* **16**, 204 (2015).
- ¹⁴ M. Ostafin and B. Nogaj, *Measurement* **40**, 43 (2007).
- ¹⁵ C. Bonhomme, C. Gervais, C. Coelho, F. Pourpoint, T. Azaïs, L. Bonhomme-Courty, F. Babonneau, G. Jacob, M. Ferrari, D. Canet, J. R. Yates, C. J. Pickard, S. A. Joyce, F. Mauri, and D. Massiot, *Magn. Reson. Chem.* **48**, S86 (2010).
- ¹⁶ D. Bräunling, O. Pecher, D. M. Trots, A. Senyshyn, D. A. Zhrebtsov, F. Haarmann, and R. Niewa, *Z. Anorg. Allg. Chem.* **636**, 936 (2010).
- ¹⁷ L. A. O'Dell, R. W. Schurko, K. J. Harris, J. Autschbach, and C. I. Ratcliffe, *J. Am. Chem. Soc.* **133**, 527 (2011).
- ¹⁸ S. Nozawa, T. Iwazumi, and H. Osawa, *Phys. Rev. B* **72**, 121101 (2005).
- ¹⁹ O. Durmeyer, E. Beaupaire, J.-P. Kappler, C. Brouder, and F. Baudelet, *J. Phys.: Condens. Matter* **22**, 125504 (2010).
- ²⁰ D. Manuel, D. Cabaret, C. Brouder, P. Saintavrit, A. Bordage, and N. Trcera, *Phys. Rev. B* **85**, 224108 (2012).
- ²¹ D. Cabaret and C. Brouder, *J. Phys.: Conf. Ser.* **190**, 012003 (2009).
- ²² C. Brouder, D. Cabaret, A. Juhin, and P. Saintavrit, *Phys. Rev. B* **81**, 115125 (2010).
- ²³ C. Gervais, L. Bonhomme-Courty, F. Mauri, F. Babonneau, and C. Bonhomme, *Phys. Chem. Chem. Phys.* **11**, 6875 (2009).
- ²⁴ N. Folliet, C. Roiland, S. Bégu, A. Aubert, T. Mineva, A. Goursot, K. Selvaraj, L. Duma, F. Tielens, F. Mauri, G. Laurent, C. Bonhomme, C. Gervais, F. Babonneau, and T. Azaïs, *J. Am. Chem. Soc.* **133**, 16815 (2011).
- ²⁵ A. L. Ankudinov and J. J. Rehr, *Phys. Scr.* **T115**, 24 (2005).
- ²⁶ T. Fujikawa, *J. Phys. Soc. Japan* **68**, 2444 (1999).
- ²⁷ T. Fujikawa, H. Sakuma, K. Niki, and D. Sébilleau, *J. Electron Spectros. Relat. Phenomena* **198**, 57 (2015).
- ²⁸ J.-N. Dumez and C. J. Pickard, *J. Chem. Phys.* **130**, 104701 (2009).
- ²⁹ I. D. Gortari, G. Portella, X. Salvatella, V. S. Bajaj, P. C. A. van der Wel, J. R. Yates, M. D. Segall, C. J. Pickard, M. C. Payne, and M. Vendruscolo, *J. Am. Chem. Soc.* **132**, 5993 (2010).
- ³⁰ M. Robinson and P. D. Haynes, *J. Chem. Phys.* **133**, 084109 (2010).
- ³¹ M. Dračinský and P. Hodgkinson, *CrystEngComm* **15**, 8705 (2013).
- ³² A. Carof, M. Salanne, T. Charpentier, and B. Rotenberg, *J. Phys. Chem. B* **118**, 13252 (2014).
- ³³ T. A. Pascal, U. Boesenberg, R. Kostecki, T. J. Richardson, T.-C. Weng, D. Sokaras, D. Nordlund, E. McDermott, A. Moewes, J. Cabana, and D. Prendergast, *J. Chem. Phys.* **140**, 034107 (2014).
- ³⁴ T. A. Pascal, C. D. Pemmaraju, and D. Prendergast, *Phys. Chem. Chem. Phys.* **17**, 7743 (2015).
- ³⁵ O. Peyrusse, *High Energy Density Phys.* **6**, 357 (2010).
- ³⁶ S. Mazevet, V. Recoules, J. Bouchet, F. Guyot, M. Harmand, A. Ravasio, and A. Benuzzi-Mounaix, *Phys. Rev. B* **89**, 100103(R) (2014).
- ³⁷ F. Dorchie, F. Festa, V. Recoules, O. Peyrusse, A. Benuzzi-Mounaix, E. Brambrink, A. Levy, A. Ravasio, M. Koenig, T. Hall, and S. Mazevet, *Phys. Rev. B* **92**, 085117 (2015).
- ³⁸ T. D. Kühne, M. Krack, F. R. Mohamed, and M. Parrinello, *Phys. Rev. Lett.* **98**, 066401 (2007).
- ³⁹ M. Dračinský and P. Hodgkinson, *Chem. Eur. J.* **20**, 2201 (2014).
- ⁴⁰ C. P. Schwartz, J. S. Uejio, R. J. Saykally, and D. Prendergast, *J. Chem. Phys.* **130**, 184109 (2009).
- ⁴¹ S. Rossano, F. Mauri, C. J. Pickard, and I. Farnan, *J. Phys. Chem. B* **109**, 7245 (2005).
- ⁴² B. Monserrat, R. J. Needs, and C. J. Pickard, *J. Chem. Phys.* **141**, 134113 (2014).
- ⁴³ J. Canche-Tello, M. C. Vargas, J. Hernández-Cobos, I. Ortega-Blake, A. Leclercq, P. L. Solarí, C. Den Auwer, and J. Mustre de Leon, *J. Phys. Chem. A* **118**, 10967 (2014).
- ⁴⁴ R. O. Jones, *Rev. Mod. Phys.* **87**, 897 (2015).
- ⁴⁵ M. Born, K. Huang, and M. Lax, *Am. J. Phys.* (Oxford University Press, Oxford, 1954).

- ⁴⁶ S. Baroni, P. Giannozzi, and E. Isaev, *Rev. Mineral. Geochemistry* **71**, 39 (2010).
- ⁴⁷ B. Fultz, *Prog. Mater. Sci.* **55**, 247 (2010).
- ⁴⁸ C. Ronchi and M. Sheindlin, *J. Appl. Phys.* **90**, 3325 (2001).
- ⁴⁹ D. Fincham, W. C. Mackrodt, and P. J. Mitchell, *J. Phys.: Condens. Matter* **6**, 393 (1994).
- ⁵⁰ J. L. Gavartin, *J. Phys.: Condens. Matter* **13**, 10873 (2001).
- ⁵¹ A. R. Oganov, M. J. Gillan, and G. D. Price, *J. Chem. Phys.* **118**, 10174 (2003).
- ⁵² A. Maradudin, E. Montroll, G. Weiss, and I. Ipatova, *Theory of lattice dynamics in the harmonic approximation* (Academic Press, New York, 1971).
- ⁵³ C. Brouder, *J. Phys.: Condens. Matter* **2**, 701 (1990).
- ⁵⁴ A. M. Flank, G. Cauchon, P. Lagarde, S. Bac, M. Janousch, R. Wetter, J.-M. Dubuisson, M. Idir, F. Langlois, T. Moreno, and D. Vantelon, *Nucl. Instruments Methods Phys. Res. B* **246**, 269 (2006).
- ⁵⁵ P. Giannozzi, S. Baroni, N. Bonini, M. Calandra, R. Car, C. Cavazzoni, D. Ceresoli, G. L. Chiarotti, M. Cococcioni, I. Dabo, A. Dal Corso, S. de Gironcoli, S. Fabris, G. Fratesi, R. Gebauer, U. Gerstmann, C. Gougousis, A. Kokalj, M. Lazzeri, L. Martin-Samos, N. Marzari, F. Mauri, R. Mazzarello, S. Paolini, A. Pasquarello, L. Paulatto, C. Sbraccia, S. Scandolo, G. Sclauzero, A. P. Seitsonen, A. Smogunov, P. Umari, and R. M. Wentzcovitch, *J. Phys.: Condens. Matter* **21**, 395502 (2009).
- ⁵⁶ J. P. Perdew, K. Burke, and M. Ernzerhof, *Phys. Rev. Lett.* **77**, 3865 (1996).
- ⁵⁷ K. Laasonen, A. Pasquarello, R. Car, C. Lee, and D. Vanderbilt, *Phys. Rev. B* **47**, 10142 (1993).
- ⁵⁸ C. J. Pickard and F. Mauri, *Phys. Rev. B* **63**, 245101 (2001).
- ⁵⁹ N. Troullier and J. L. Martins, *Phys. Rev. B* **43**, 1993 (1991).
- ⁶⁰ I. Errea, M. Calandra, and F. Mauri, *Phys. Rev. Lett.* **111**, 177002 (2013).
- ⁶¹ I. Errea, M. Calandra, and F. Mauri, *Phys. Rev. B* **89**, 064302 (2014).
- ⁶² R. Hazen, *Am. Mineral.* **61**, 266 (1976).
- ⁶³ R. R. Reeber, K. Goessel, and K. Wang, *Eur. J. Mineral.* **7**, 1039 (1995).
- ⁶⁴ H. J. Monkhorst and J. D. Pack, *Phys. Rev. B* **13**, 5188 (1976).
- ⁶⁵ X. Gonze, *Phys. Rev. A* **52**, 1096 (1995).
- ⁶⁶ S. Baroni, S. de Gironcoli, A. Dal Corso, and P. Giannozzi, *Rev. Mod. Phys.* **73**, 515 (2001).
- ⁶⁷ X. Gonze and C. Lee, *Phys. Rev. B* **55**, 10355 (1997).
- ⁶⁸ J. R. Yates, C. J. Pickard, and F. Mauri, *Phys. Rev. B* **76**, 024401 (2007).
- ⁶⁹ P. Pyykkö, *Mol. Phys.* **106**, 1965 (2008).
- ⁷⁰ M. Taillefumier, D. Cabaret, A. M. Flank, and F. Mauri, *Phys. Rev. B* **66**, 195107 (2002).
- ⁷¹ C. Gougousis, M. Calandra, A. P. Seitsonen, and F. Mauri, *Phys. Rev. B* **80**, 075102 (2009).
- ⁷² T. Mizoguchi, I. Tanaka, S.-P. Gao, and C. J. Pickard, *J. Phys.: Condens. Matter* **21**, 104204 (2009).
- ⁷³ P. Jiang, D. Prendergast, F. Borondics, S. Porsgaard, L. Giovanetti, E. Pach, J. Newberg, H. Bluhm, F. Besenbacher, and M. Salmeron, *J. Chem. Phys.* **138**, 024704 (2013).
- ⁷⁴ G. Lelong, G. Radtke, L. Cormier, H. Bricha, J.-P. Rueff, J. M. Ablett, D. Cabaret, F. Gélébart, and A. Shukla, *Inorg. Chem.* **53**, 10903 (2014).
- ⁷⁵ M. Profeta, M. Benoit, F. Mauri, and C. J. Pickard, *J. Am. Chem. Soc.* **126**, 12628 (2004).
- ⁷⁶ L. He, F. Liu, G. Hautier, M. J. T. Oliveira, M. A. L. Marques, F. D. Vila, J. J. Rehr, G.-M. Rignanese, and A. Zhou, *Phys. Rev. B* **89**, 064305 (2014).
- ⁷⁷ Z. Wu and R. E. Cohen, *Phys. Rev. B* **73**, 235116 (2006).
- ⁷⁸ J. P. Perdew, A. Ruzsinszky, G. I. Csonka, O. A. Vydrov, G. E. Scuseria, L. A. Constantin, X. Zhou, and K. Burke, *Phys. Rev. Lett.* **100**, 136406 (2008).
- ⁷⁹ R. Laskowski, P. Blaha, and F. Tran, *Phys. Rev. B* **87**, 195130 (2013).
- ⁸⁰ R. M. Wentzcovitch, Z. Wu, and P. Carrier, *Rev. Mineral. Geochemistry* **71**, 99 (2010).
- ⁸¹ B. Monserrat, N. D. Drummond, and R. J. Needs, *Phys. Rev. B* **87**, 144302 (2013).
- ⁸² M. L. Bortz, R. H. French, D. J. Jones, R. V. Kasowski, and F. S. Ohuchi, *Phys. Scr.* **41**, 537 (1990).
- ⁸³ R. French, R. V. Kasowski, F. Ohuchi, D. J. Jones, H. Song, and R. Coble, *J. Am. Ceram. Soc.* **73**, 3195 (1990).
- ⁸⁴ W. L. O'Brien, J. Jia, Q.-Y. Dong, T. A. Callcott, D. R. Mueller, and D. L. Ederer, *Phys. Rev. B* **45**, 3882 (1992).
- ⁸⁵ C. R. Natoli, in *EXAFS near-edge Struct. III* (Springer, Berlin Heidelberg, 1984) pp. 38–42.
- ⁸⁶ G. Antonius, S. Poncé, P. Boulanger, M. Côté, and X. Gonze, *Phys. Rev. Lett.* **112**, 215501 (2014).
- ⁸⁷ S. Poncé, G. Antonius, Y. Gillet, P. Boulanger, J. Laflamme Janssen, A. Marini, M. Côté, and X. Gonze, *Phys. Rev. B* **90**, 214304 (2014).
- ⁸⁸ A. Marini, S. Poncé, and X. Gonze, *Phys. Rev. B* **91**, 224310 (2015).
- ⁸⁹ S. Poncé, Y. Gillet, J. Laflamme Janssen, A. Marini, M. J. Verstraete, and X. Gonze, *J. Chem. Phys.* **143**, 102813 (2015).
- ⁹⁰ R. Nemausat, C. Brouder, C. Gervais, and D. Cabaret, *J. Phys.: Conf. Ser.* (submitted).
- ⁹¹ R. G. Newton, *Scattering theory of waves and particles*, 2nd ed. (Springer, New York, 1982) p. 177.
- ⁹² M. O. Krause and J. H. Oliver, *J. Phys. Chem. Ref. Data* **8**, 329 (1979).
- ⁹³ K. K. Irikura, *J. Phys. Chem. Ref. Data* **36**, 389 (2007).
- ⁹⁴ R. D. Cowan, *The Theory of Atomic Structure and Spectra* (University of California Press, 1981).